Supporting Information

Surface Cobaltization for Boosted Kinetics and Excellent Stability of Nickel-rich Layered Cathodes

Qiusheng Zhang,[1] *Chunyu Cui,*[1] *Hao Chen,*[1] *Shuaijun Pan,*[1] *Yinghe Zhang*[2] *,Jian Zhu* [1,3]* *and Bingan Lu*[1]*

[1]State Key Laboratory for Chemo/Biosensing and Chemometrics, College of Chemistry and Chemical Engineering, Hunan Key Laboratory of Two-Dimensional Materials, School of Physics and Electronics, Hunan University, Changsha, 410082 (P. R. China)

[2]School of science, Harbin Institute of Technology, Shenzhen, 518055 (P. R. China).

[3]Shenzhen Research Institute, Hunan University, Changsha, 518055 (P. R. China).

[*]*Corresponding authors: jzhu@hnu.edu.cn, luba2012@hnu.edu.cn*

This file includes:

Supporting Text

Computational methods

The Vienna ab initio simulation package (VASP) was employed with the Perdew-Burke-Ernzerh (PBE) form of the generalized gradient approximation (GGA)[1,2,3]. The plane-wave projector-augmented wave method was used in the all calculations[4,5]. The PBE+U method with spin polarization is applied to calculate both structural and electronic properties[6]. The specific U values are set as follows: 3.5 eV for Mn, 3.3 eV for Co, and 6.4 eV for Ni. The selection of U values and the construction of the $LiNi_{0.6}Mn_{0.4}O_2$ model were based on computational data available from the Materials Project Website (https://www.materialsproject.org/). The Brillouin zone was sampled using a Monkhorst-Pack k-point grid of 4 × 2 × 2. A supercell model of 120 atoms containing 30 formula units was used, and a Ni atom was substituted with a Co atom as an approximate model for the Co-NM64 cathode.

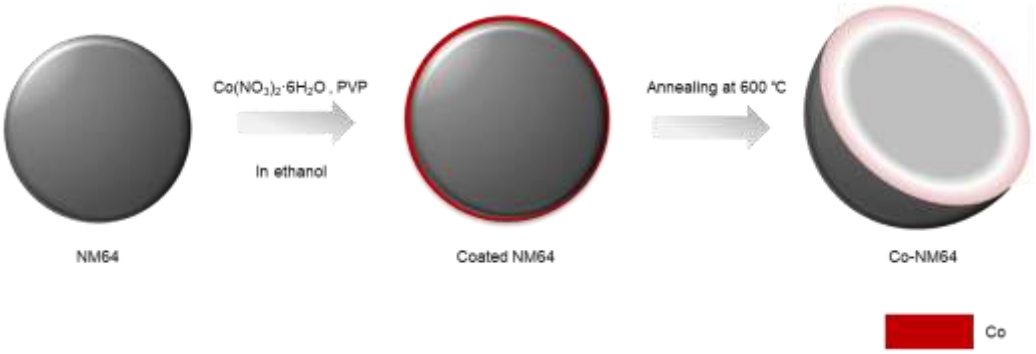

Figure S1. Schematic synthesis route of the surface cobaltization of Co-NM64 cathode material.

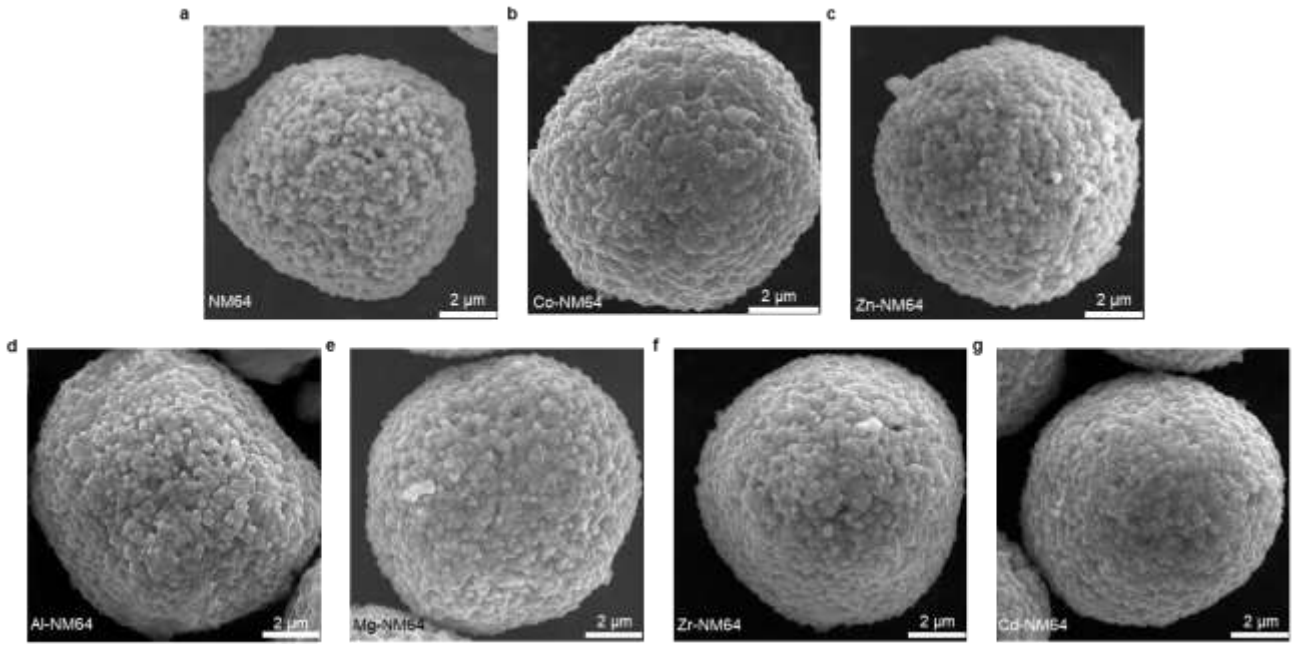

Figure S2. Lower-magnification SEM images of pristine NM64 (**a**), Co-NM64 (**b**), Zn-NM64 (**c**), Al-NM64 (**d**), Mg-NM64 (**e**), Zr-NM64 (**f**) and Cd-NM64 (**g**).

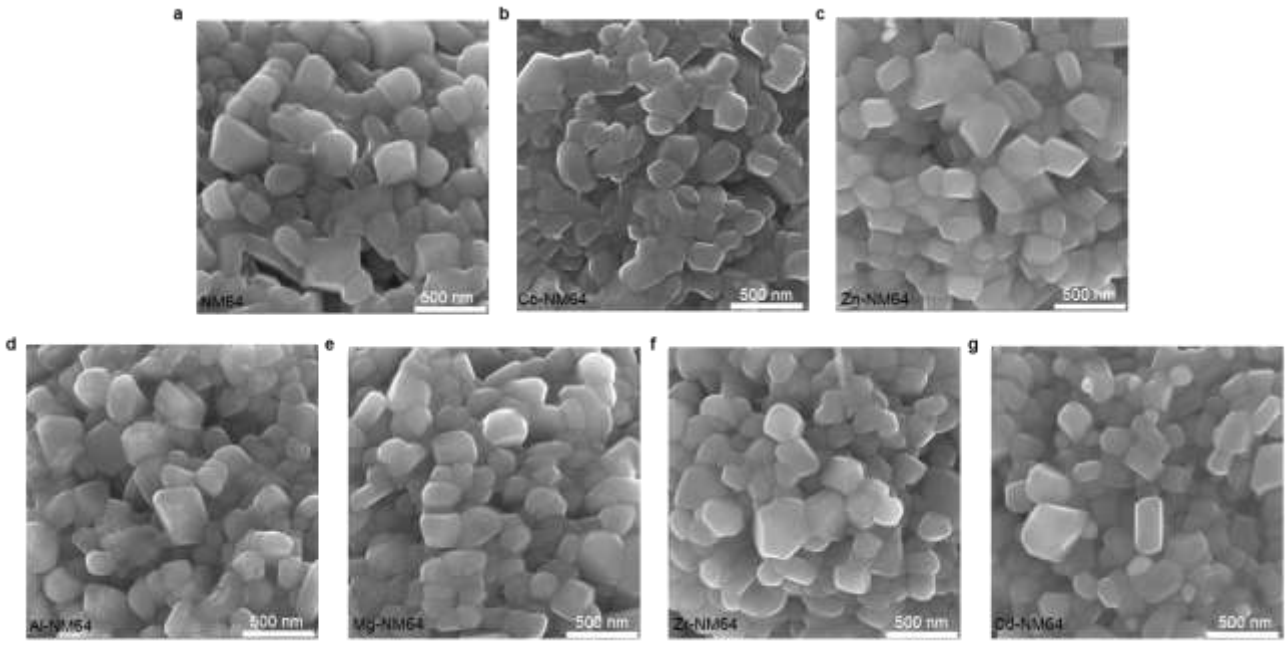

Figure S3. SEM images of NM64 (**a**), Co-NM64 (**b**), Zn-NM64 (**c**), Al-NM64 (**d**), Mg-NM64 (**e**), Zr-NM64 (**f**) and Cd-NM64 (**g**).

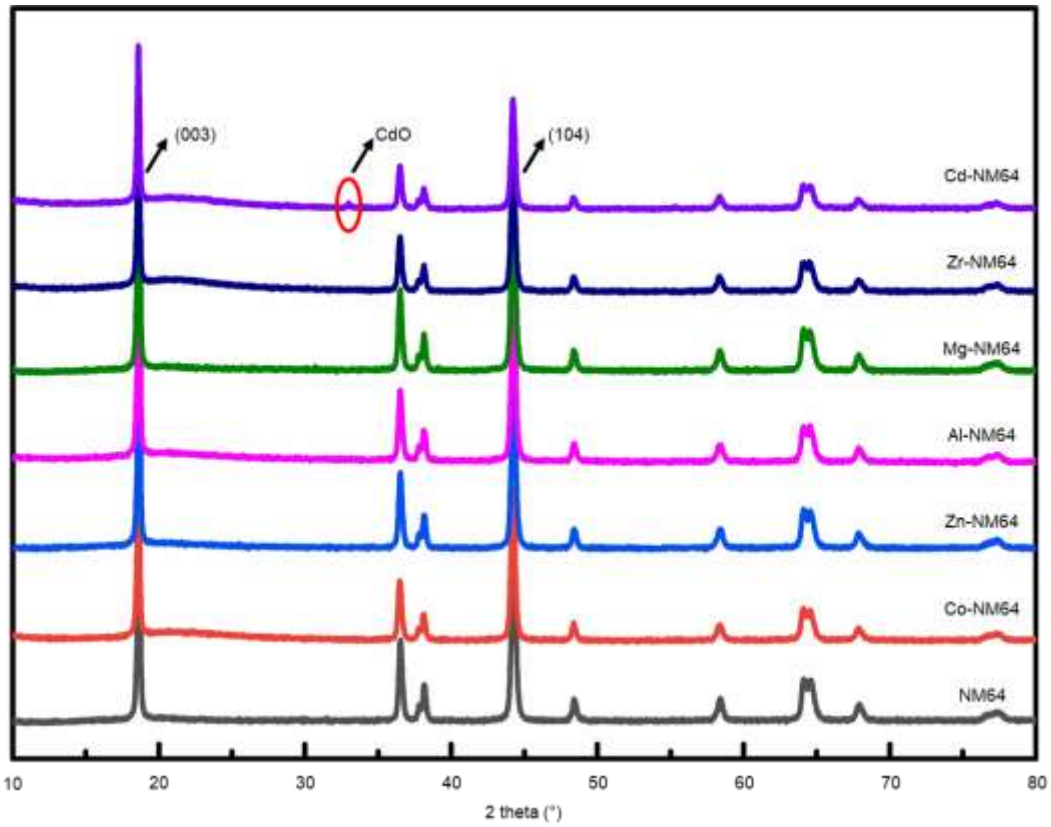

Figure S4. XRD characterizations of NM64, Co-NM64, Zn-NM64, Al-NM64, Mg-NM64, Zr-NM64 and Cd-NM64.

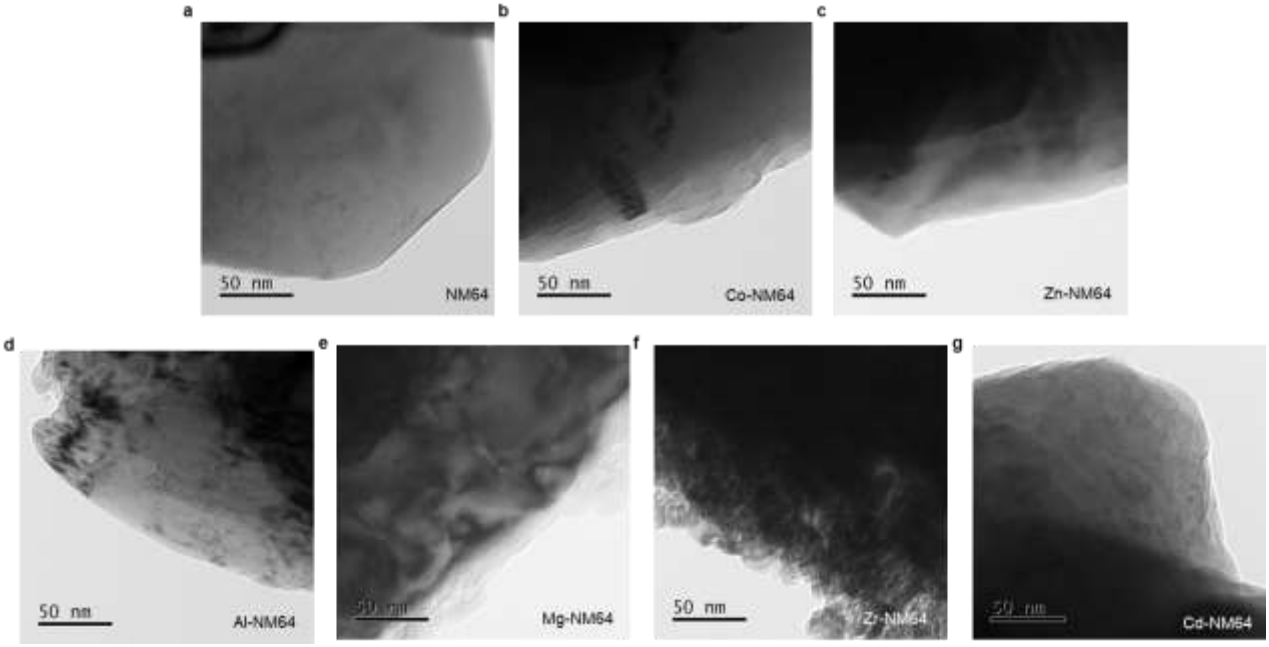

Figure S5. TEM images of NM64 (**a**), Co-NM64 (**b**), Zn-NM64 (**c**), Al-NM64 (**d**), Mg-NM64 (**e**), Zr-NM64 (**f**) and Cd-NM64 (**g**).

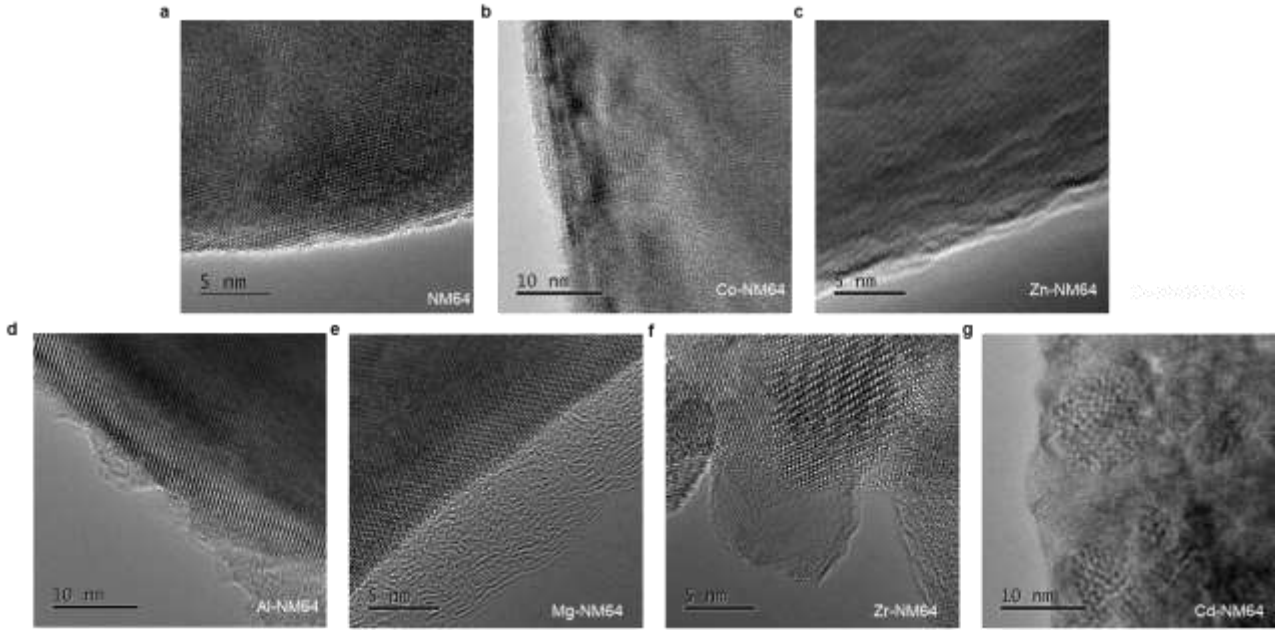

Figure S6. HRTEM images of NM64 (**a**), Co-NM64 (**b**), Zn-NM64 (**c**), Al-NM64 (**d**), Mg-NM64 (**e**), Zr-NM64 (**f**) and Cd-NM64 (**g**).

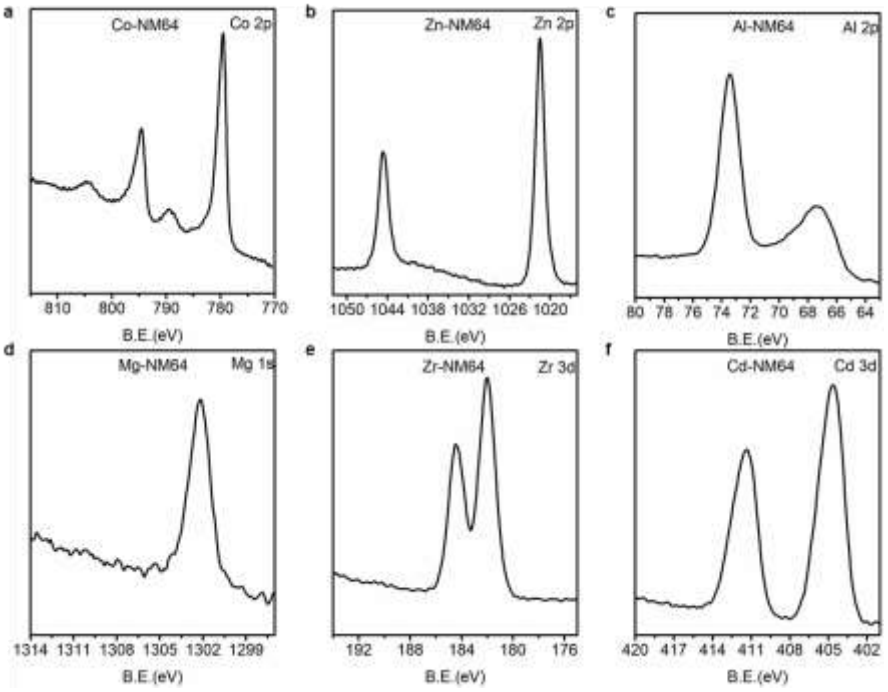

Figure S7. XPS spectra of the coated elements for Co-NM64 (**a**), Zn-NM64 (**b**), Al-NM64 (**c**), Mg-NM64 (**d**), Zr-NM64 (**e**), Cd-NM64 (**f**).

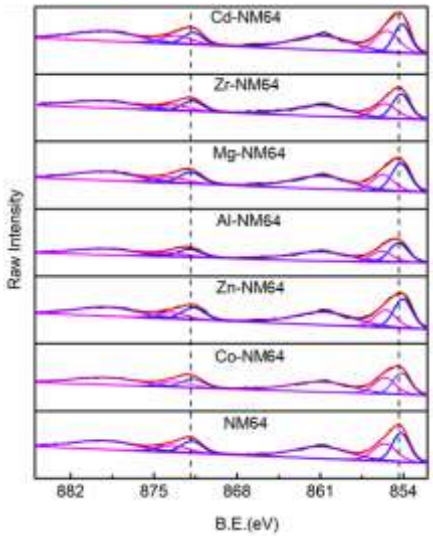

Figure S8. XPS spectra of Ni 2p for NM64, Co-NM64, Zn-NM64, Al-NM64, Mg-NM64, Zr-NM64 and Cd-NM64.

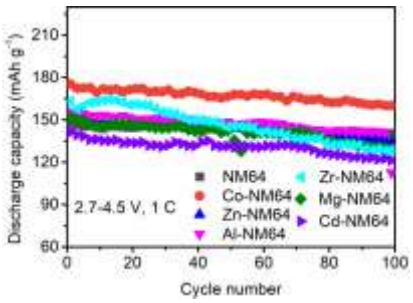

Figure S9. Cycling performance of NM64 surface modification by different elements within a voltage window of 2.7-4.5 V versus Li/Li^+.

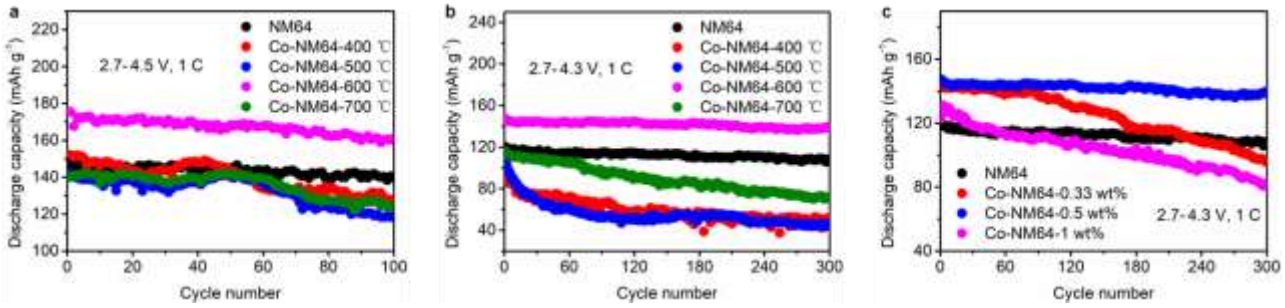

Figure S10. a,**b** Cycle performance at different annealing temperatures at a rate of 1 C within 2.7–4.3 V (**a**) and 2.7–4.5 V (**b**) versus Li. **c** Cycle performance at different Co contents at a rate of 1 C within 2.7–4.3 V versus Li.

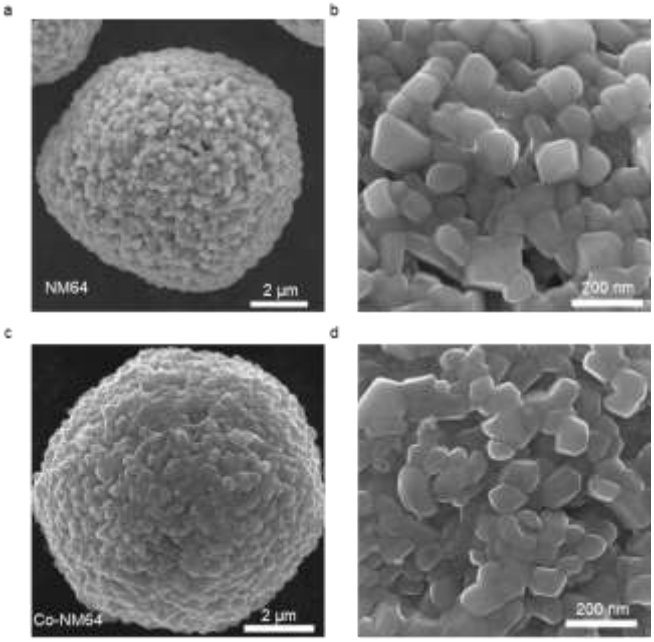

Figure S11. SEM images of pristine NM64 (**a**,**b**) and Co-NM64 (**c**,**d**).

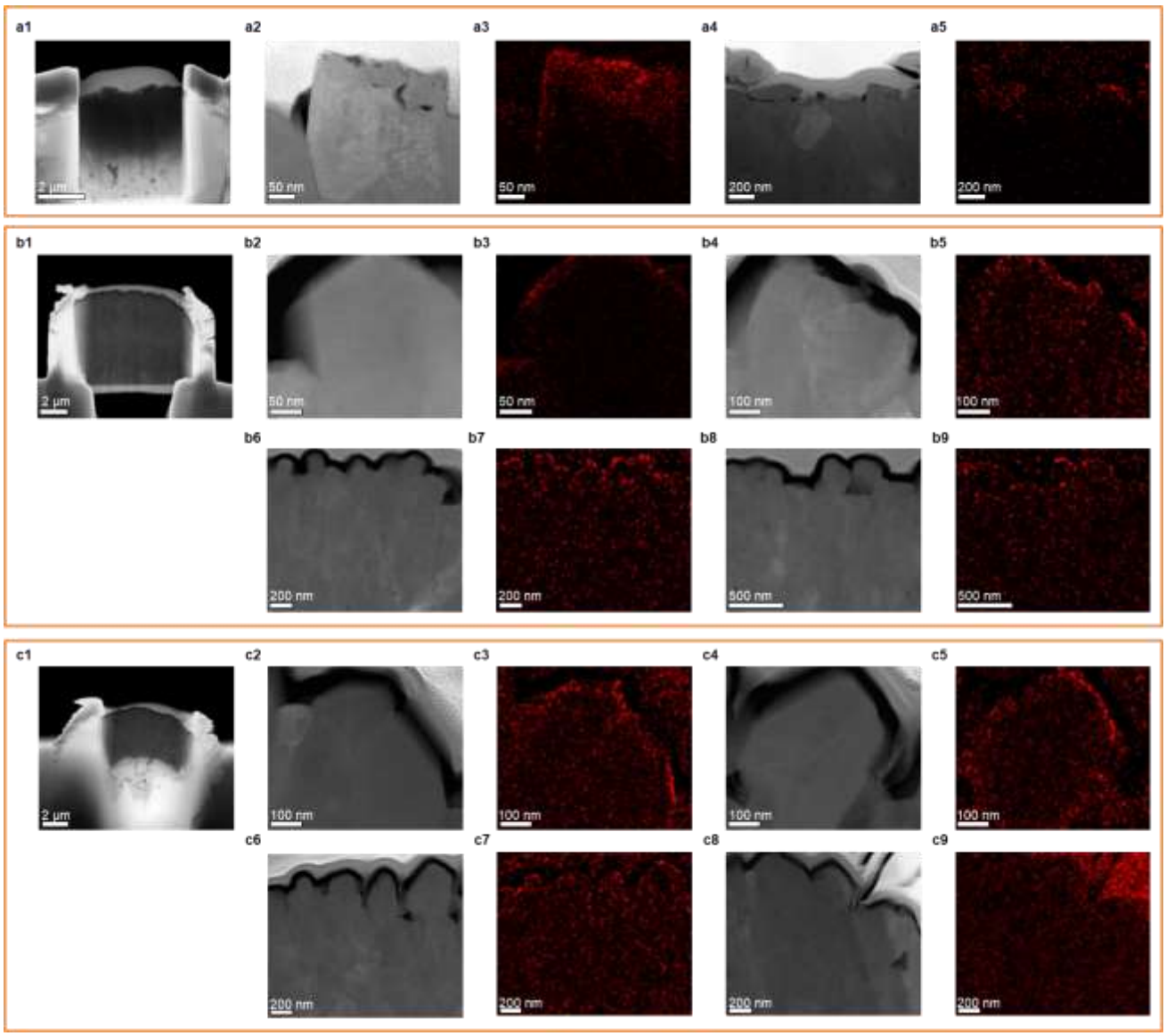

Figure S12. Three set of TEM results about the distribution of Co elements on the surface. (a1-a5) First set of HADDF-STEM images of Co-NM64 and the corresponding Co EDX mapping. (b1-b9) Second set of HADDF-STEM images of Co-NM64 and the corresponding Co EDX. (c1-b9) Third set of HADDF-STEM images of Co-NM64 and the corresponding Co EDX mapping.

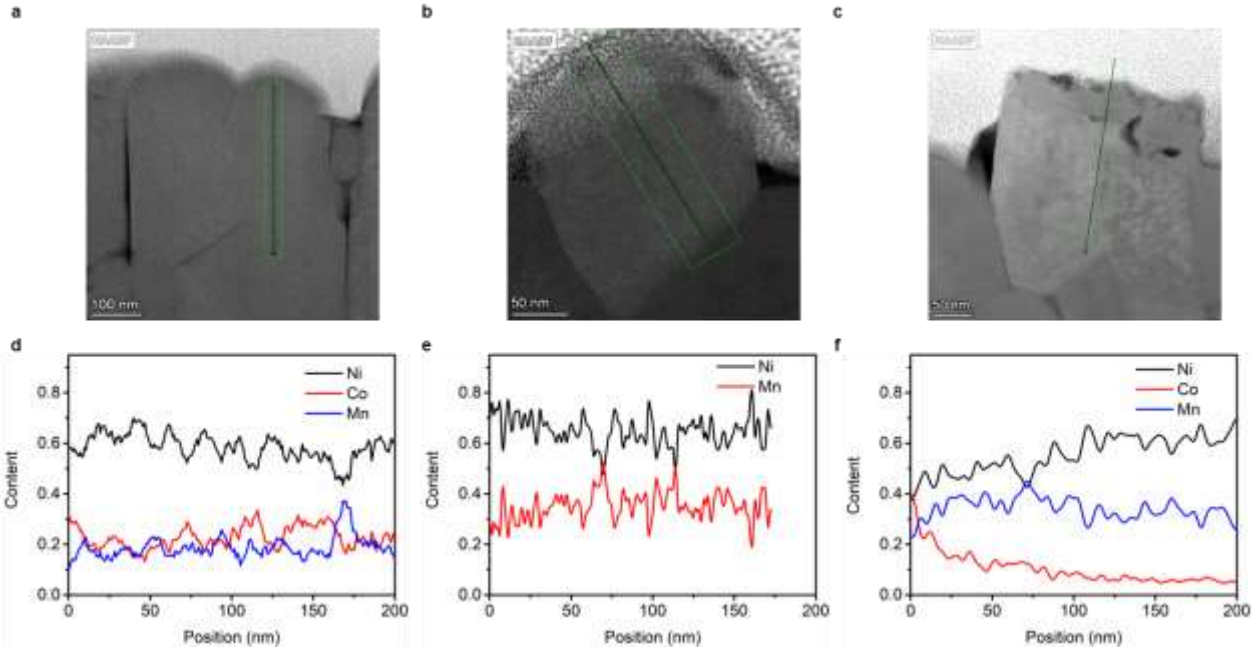

Figure S13. a-c STEM cross sectional images of NCM622 (**a**), NM64 (**b**) and Co-NM64 (**c**). **d-f**, EDS line profile of Ni, Co and Mn distribution along their respective black arrows of NCM622 (**d**), NM64 (**e**) and Co-NM64 (**f**).

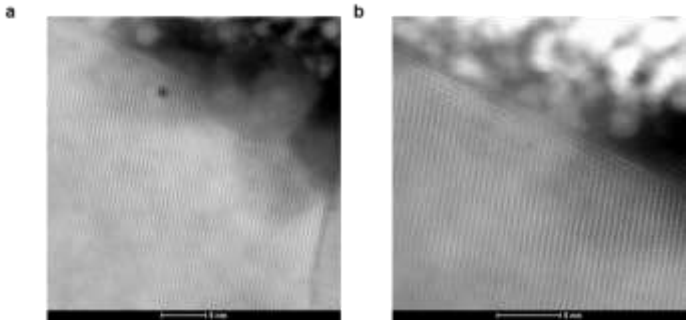

Figure S14. a,**b** HAADF-STEM images of different regions on the Co-NM64 surface.

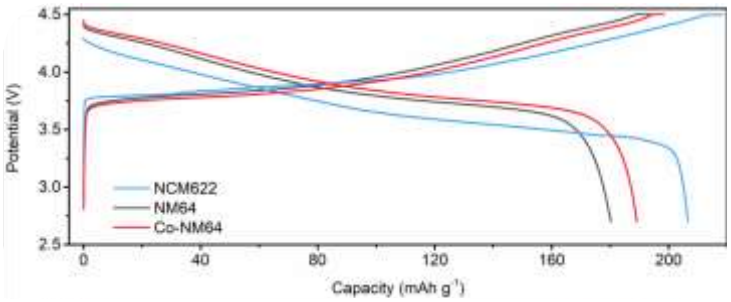

Figure S15. Initial charge-discharge curves of NCM622,NM64 and Co-NM64 with a CCCV mode (0.1 C//0.05 C, 4.5 V) in the range of 2.7-4.5 V versus Li/Li^+.

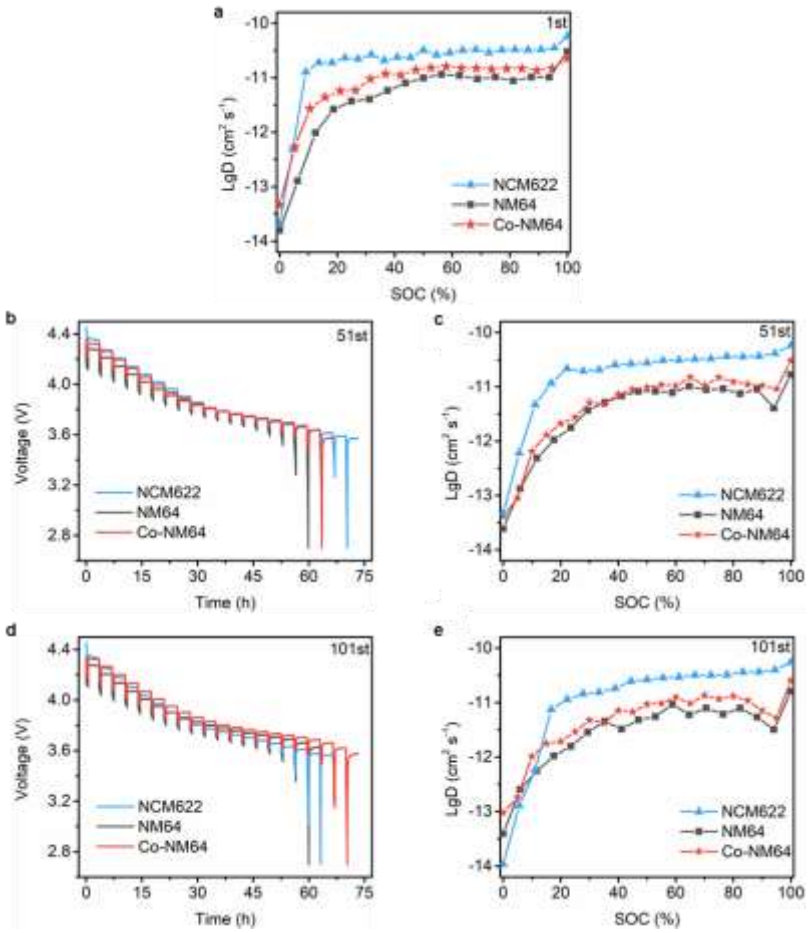

Figure S16. a,**c**,**e** Li^+ diffusion coefficients of NCM622, NM64 and Co-NM64 at 1st (**a**), 51st (**c**) and 101st (**e**). **b**,**d** Discharge curves of the GITT measurements at a current density of 0.1 C at 51st (**b**) and 101st (**d**).

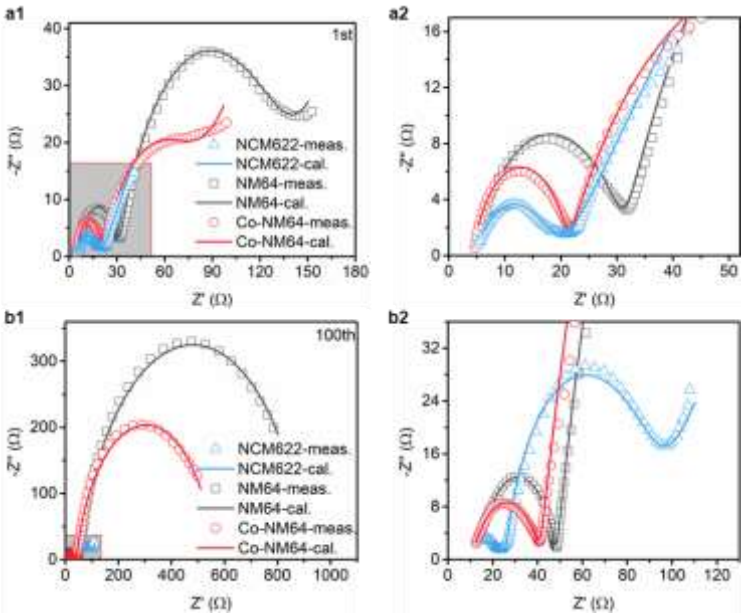

Figure S17. a1,**a2,b1,b2** Nyquist plots and fitting curves of NCM622, NM64 and Co-NM64 after activation (**a1,a2**) and 100 cycles (**b1,b2**) at the charged state (4.0 V).

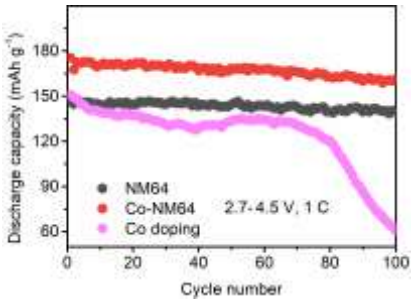

Figure S18 Cycle performance of Co doping NM64 at a rate of 1 C within 2.7–4.5 V versus Li/Li^+.

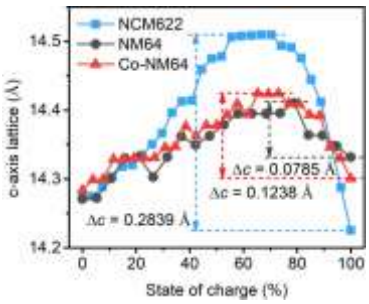

Figure S19. Change in *c*-axis lattice parameters of NCM622, NM64 and Co-NM64 during charging

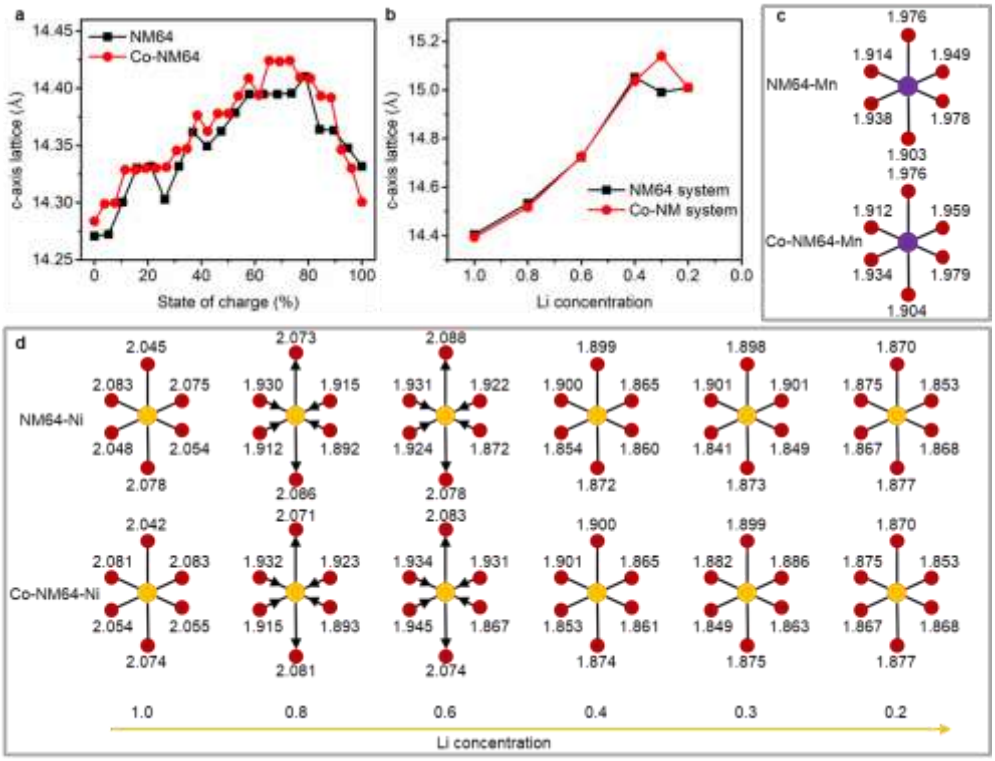

Figure S20. (a) The *c*-lattice evolution calculated from in situ XRD. (b) Calculated ab initio *c*-lattice parameters (c) Calculated Mn-O bonds in Mn-O octahedra under full lithiation. The same Mn atoms sites are selected for NM64 and Co-NM systems. (d) Calculated Ni-O bonds in Ni-O octahedra under different Li concentration. The same Ni atoms sites are selected for NM64 and Co-NM systems

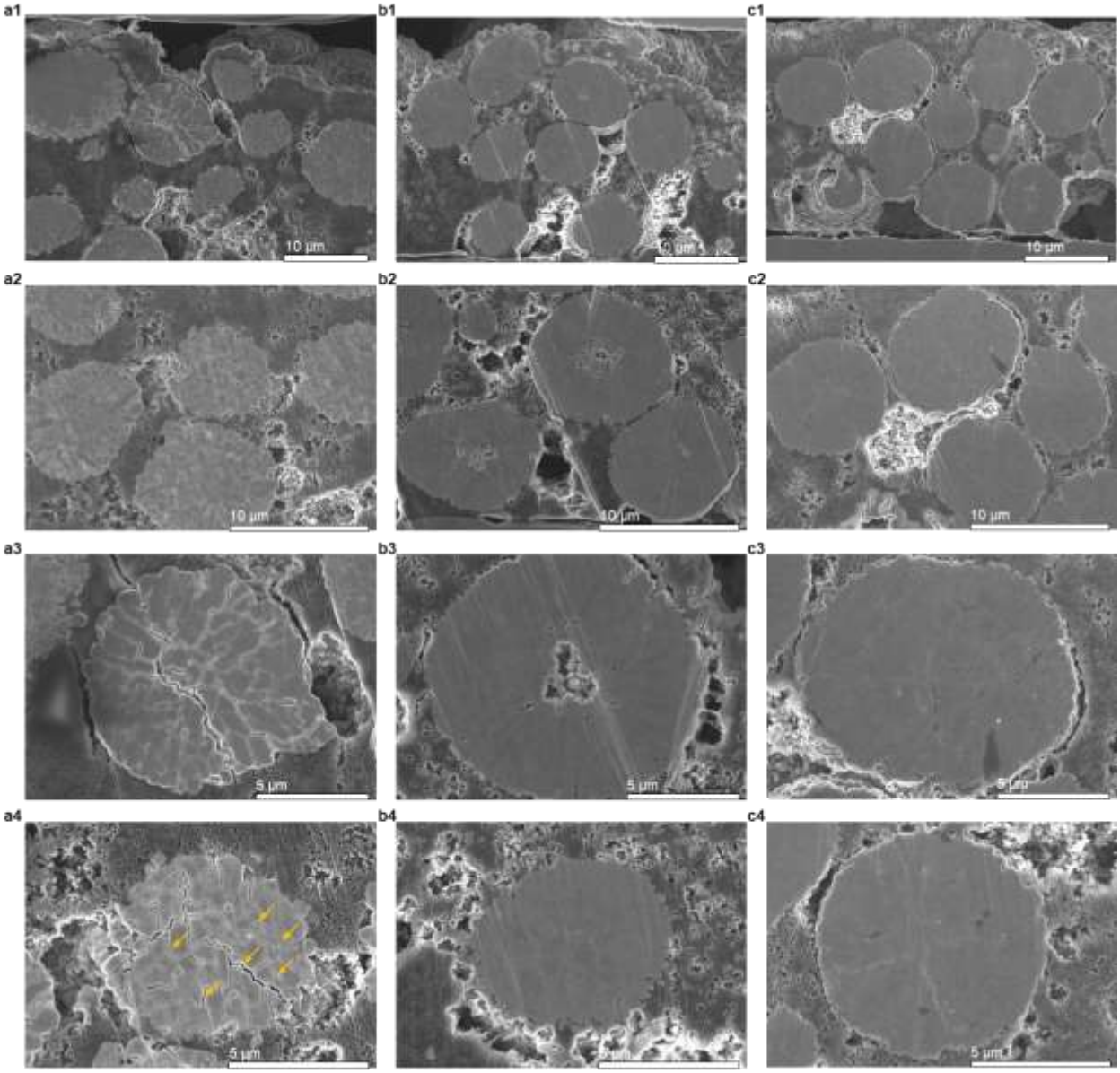

Figure S21 The cross-section FEB-SEM images of the electrodes of (a1-a4) NMC622, (b1-b4) NM64 and (c1-c4) Co-NM64 charged to 4.5 V after 100 cycles in the 2.7–4.5 V (vs. Li/Li^+) voltage range.

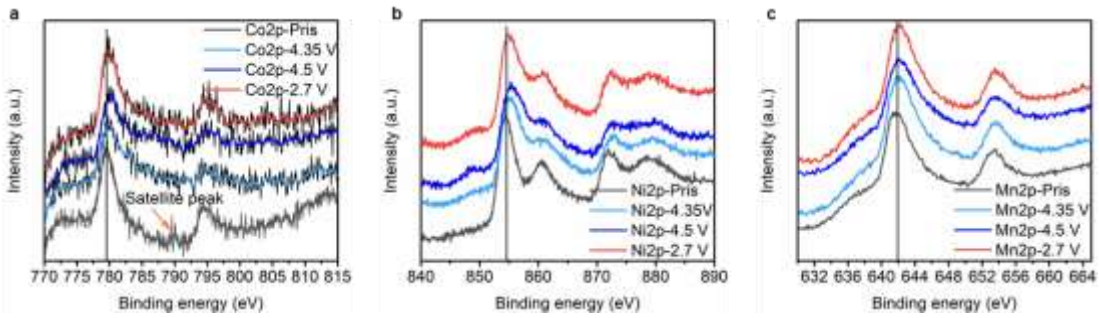

Figure S22. *Ex-situ* Co2p (a), Ni2p (b) and Mn2p (c) XPS spectra of Co-NM64.

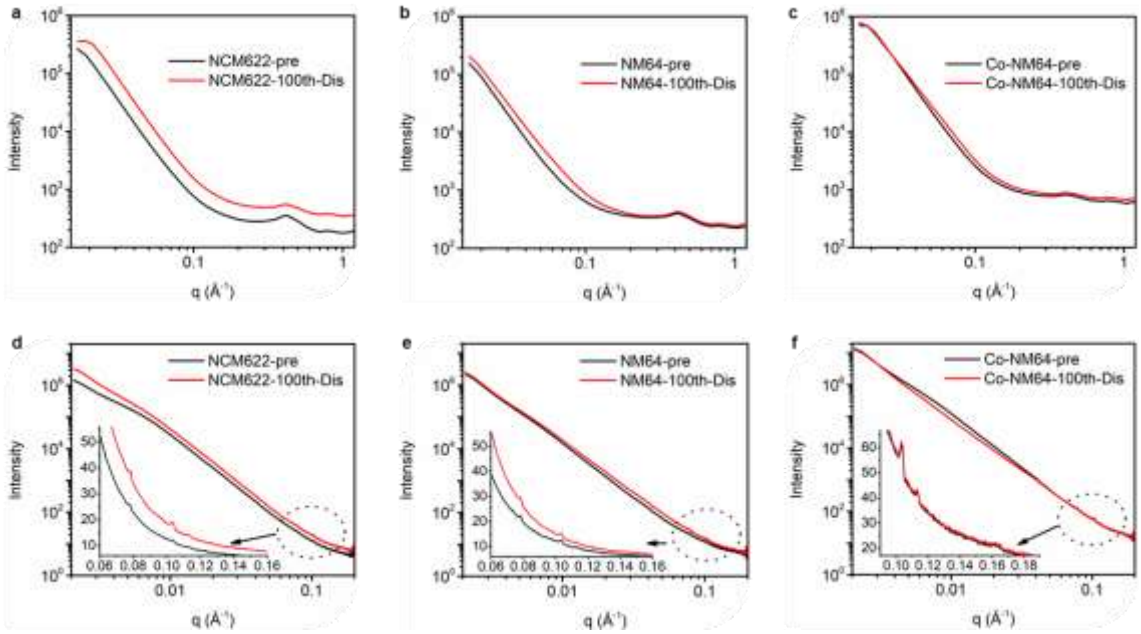

Figure S23. High-throughput characterization of the stability of NCM622, NM64 and Co-NM64. **a-c** Synchrotron small-angle X-ray scattering (SAXS) at high Q region for NCM622 (**a**), NM64 (**b**) and Co-NM64 (**c**). **d-f** Synchrotron SAXS in middle Q region for NCM622 (**d**), NM64 (**e**) and Co-NM64 (**f**).

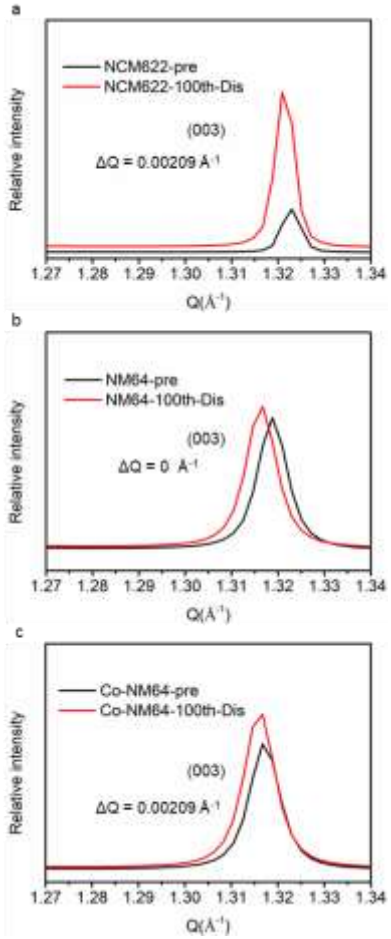

Figure S24. Synchrotron small-angle X-ray scattering (saxs) at high Q region for NCM622 (**a**), NM64 (**b**) and Co-NM64 (**c**).

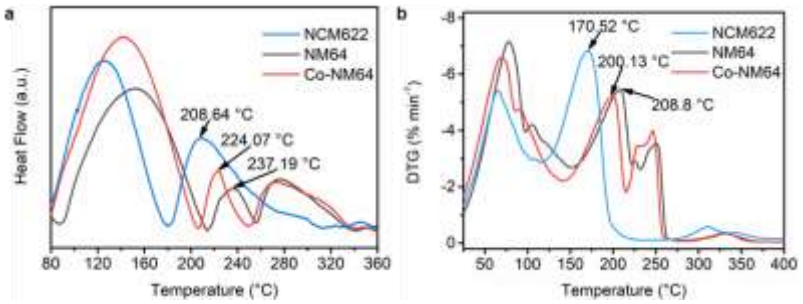

Figure S25. DSC measurement (**a**) and DTG (**b**) of NCM622, NM64 and Co-NM64 charged to 4.5 V.

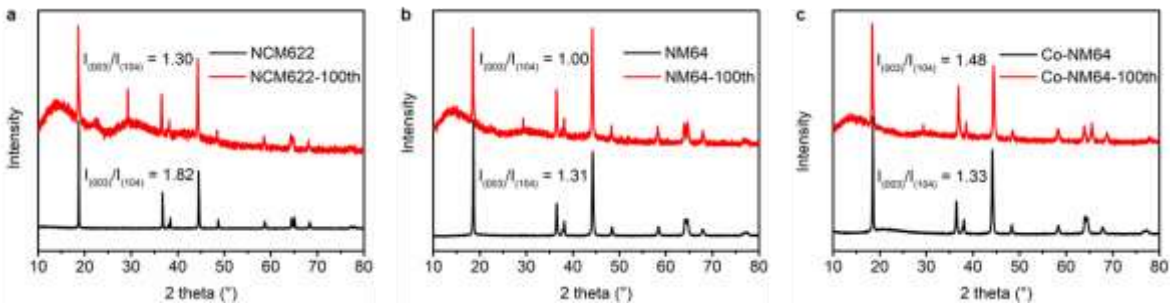

Figure S26. XRD patterns of NCM622 (**a**), NM64 (**b**) and Co-NM64 (**c**) before and after cycling.

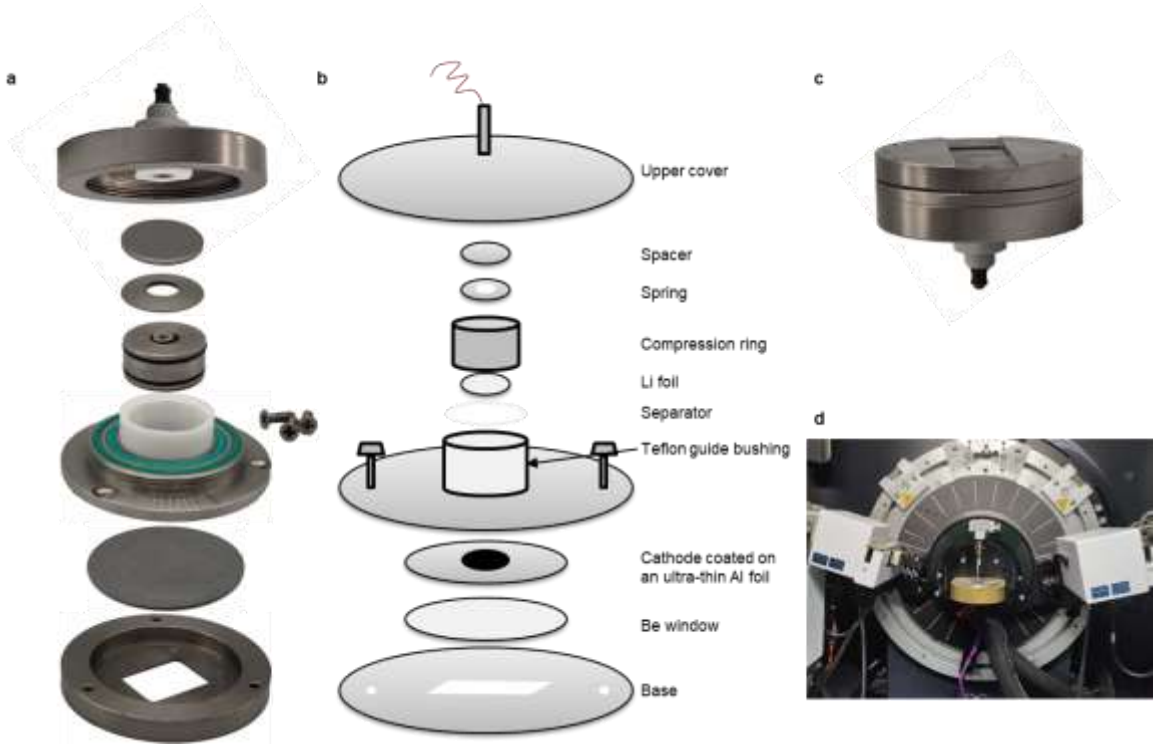

Figure S27. (a,c) The physical pictures and (b) schematic diagram of the *in-situ* XRD cell. (d) The powder diffractometer equipped with the *in-situ* XRD cell.

Supporting Table 1. Particle size distribution of NCM622, NM64 and Co-NM64.

Sample	Particle size distribution		
	D_{10}(μm)	D_{50}(μm)	D_{90}(μm)
NCM622	7.270	13.489	23.225
NM64	6.869	9.477	13.051
Co-NM64	6.760	9.289	12.728

Supporting Table 2. The fitted results by the equivalent circuit of NCM622, NM64 and Co-NM64.

Sample	1 cycle			100 cycles		
	R_{sol}	R_f	R_{ct}	R_{sol}	R_f	R_{ct}
NCM622(Ω)	4.2337	10.578	9.4608	9.2786	17.558	64.308
NM64(Ω)	4.6873	26.469	106.42	14.212	34.075	864.38
Co-NM64(Ω)	4.3165	16.843	64.555	10.696	30.806	523.31

Supporting Table 3. The refinement result of the XRD measurements of NCM622, NM64 and Co-NM64.

Samples	*a*(*b*)	*c*	Li/Ni disorder	R_{wp}	CHI^2
NCM622	2.8744 Å	14.2476 Å	4.7%	0.0631	1.063
NM64	2.8887 Å	14.3048 Å	9.0%	0.0201	1.380
Co-NM64	2.8854 Å	14.2895 Å	9.3%	0.0213	1.296

Samples	Element	Wyckoff site	*x*	*y*	*z*	Occupancy
NCM622	Ni1	3b	0	0	0.5	0.553(3)
	Co1	3b	0	0	0.5	0.2
	Mn1	3b	0	0	0.5	0.2
	Li2	3b	0	0	0.5	0.046(7)
	Li1	3a	0	0	0	0.953(3)
	Ni2	3a	0	0	0	0.046(7)
	O	6c	0	0	0.258100	1
NM64	Ni1	3b	0	0	0.5	0.510(1)
	Mn1	3b	0	0	0.5	0.4
	Li2	3b	0	0	0.5	0.089(9)
	Li1	3a	0	0	0	0.910(1)
	Ni2	3a	0	0	0	0.089(9)
	O	6c	0	0	0.243245	1
Co-NM64	Ni1	3b	0	0	0.5	0.507(1)
	Mn1	3b	0	0	0.5	0.4
	Li2	3b	0	0	0.5	0.092(9)
	Li1	3a	0	0	0	0.907(1)
	Ni2	3a	0	0	0	0.092(9)
	O	6c	0	0	0.243867	1

Supporting Table 4. The detailed testing conditions for each full cell ever reported. The red font corresponds to the data in Fig. 5c.

Material	Initial capacity (mAh g^{-1})	Capacity retention (%)	Cycle number	Capacity retention per 100 cycles (%)	C-rate ($mA\ g^{-1}$)	Voltage Range (V)	Test temperature (°C)	cathode||electrolyte||anode	Ref.
NCM523	1000 mAh	78	600	96.3	1C	2.75-4.2	25	NCM523||1 M $LiPF_6$ in EC/EMC/DEC(3:5:2, in weight)+1wt % NOB||artificial graphite	7
NCM523	182.6	83	200	91.5	1C(151.1)	3-4.3	30	NCM523||1.2 M $LiPF_6$ in EC:EMC, 3:7 wt/wt (Gen2) electrolyte||graphite	8
NCM523	163	97	100	97.0	1C(170)	2.8-4.3	20	NCM523||1 M $LiPF_6$ in EC/EMC 3 : 7 by wt||graphite	9
NCM523	240 mAh	96	4000	99.9	1C	3-4.3	20	NMC532||1.2 M (2FEC+1LFO)||graphite	10
NCM523	175	56.2	400	89.1	1C(180)	3.0–4.4	30	NCM523||EC:EMC (3:7 by wt) + 1.2 M $LiPF_6$–based (Gen2) electrolyte||graphite	11
NCM523	194.2	68.38	200	84.2	1C(151.1)	3.0–4.4	30	NCM523||1.2 M $LiPF_6$ in EC:EMC, 3:7 wt/wt (Gen2)||graphite	8
NCM523	1900 mAh	77.7	250	91.1	0.5C	3.0–4.4	25	NCM523||1.0 M $LiPF_6$/EC: EMC:DEC (30:50:20 wt%)+1.0wt% VC||artificial graphite	12
NCM523	2200 mAh	93	150	95.3	1C	2.75-4.4	25	NCM523||1 M $LiPF_6$ in EC/EMC 3:7 by wt + 2% $LiPO_2F_2$ additive||artificial graphite	13
NCM523	2200 mAh	89	150	92.7	1C	2.75-4.4	25	NCM523||1 M $LiPF_6$ in EC/EMC 3:7 by wt+1 wt% D-DTD||artificial graphite	14
NCM622	155.4	95	300	98.3	1C(160)	3.0-4.2	25	NCM622||1 M $LiPF_6$ in EC:EMC 3:7 wt/wt||graphite	15
NCM622	157.5	80	1375	98.5	1C(200)	3.0-4.2	25	NCM622||1.1 M $LiPF_6$ in EC:EMC:DEC (3:5:2 vol%)+1%wt VC+1%wt DTD+0.5%wt LiFSI+0.5% $LiPO_2F_2$||graphite	16
NCM622	154	92	312	97.4	1C(155)	3.0-4.2	25	NCM622||1 M $LiPF_6$ in EC:EMC 3:7 wt/wt||graphite	17
NCM622	165	91	312	97.1	1C(165)	3.0-4.3	25	NCM622||1 M $LiPF_6$ in EC:EMC 3:7 wt/wt||graphite	17
NCM622	174	84	312	94.9	1C(175)	3.0-4.4	25	NCM622||1 M $LiPF_6$ in EC:EMC 3:7 wt/wt||graphite	17
NCM622	175	80	345	94.2	1C(200)	3.0-4.4	25	NCM622||1.1 M $LiPF_6$ in EC:EMC:DEC (3:5:2 vol%)+1%wt VC+1%wt DTD+0.5%wt LiFSI+0.5% $LiPO_2F_2$||graphite	16
NCM622	177.8	94	300	98.0	1C(180)	3.0–4.4	25	NCM622||1 M $LiPF_6$ in EC:EMC 3:7 wt/wt||graphite	15
NCM811	172.5	66	300	88.7	1C(170)	3.0-4.2	25	NCM811||1 M $LiPF_6$ in EC:EMC 3:7 wt/wt||graphite	15
NCM811	169.2	78	1000	97.8	1C(180)	2.5-4.2	25	NCM811||1 M $LiPF_6$ in EC:EMC 3:7 wt/wt+ 2%VC||MCMB graphite	18
NCM811	186.8	83.7	400	95.9	1C(188.4)	3.0-4.3	25	NCM811||1.15 M $LiPF_6$ in EC/EMC/DMC(3:4:3 vol%)+5 wt% FEC||graphite	19
NCM811	184.6	52	1000	95.2	1C(180)	2.5-4.4	25	NCM811||1 M $LiPF_6$ in EC:EMC 3:7 wt/wt+ 2%VC||MCMB graphite	18
NCM811	202.9	79	300	93.0	1C(180)	2.75-4.4	25	NCM811||1.0 M $LiPF_6$ dissolved in SL/FEC/EMC (1:1:3, v/v/v) with 0.5 wt % $LiBF_4$−$LiNO_3$||graphite	20
This work	154.5	90.5	300	96.8	1C(180)	2.7-4.4	30	NM64||1.2 M $LiPF_6$ in EC:EMC 3:7 vol/vol||graphite	/

Supporting References

1. Kresse, G., & Furthmüller, J.. Efficient iterative schemes for ab initio total-energy calculations using a plane-wave basis set. *Phys. Rev. B*, **54**, 11169 (1996).
2. Kresse, G., & Furthmüller, J. Efficiency of ab-initio total energy calculations for metals and semiconductors using a plane-wave basis set. *Comput. Mater. Sci.*, **6**, 15-50 (1996).
3. Perdew, J. P., Burke, K., & Ernzerhof, M. Generalized gradient approximation made simple. *Phys. Rev. L*, **77**, 3865 (1996).
4. Blöchl, P. E. Projector augmented-wave method. *Phys. Rev. B*, **50**, 17953 (1994).
5. Kresse, G., & Joubert, D. From ultrasoft pseudopotentials to the projector augmented-wave method. *Phys. Rev. B*, **59**, 1758 (1999).
6. Anisimov, V. I., Zaanen, J., & Andersen, O. K. Band theory and Mott insulators: Hubbard U instead of Stoner I. *Phys. Rev. B*, **44**, 943 (1991).
7. Hu, Z. et al. A novel electrolyte additive enables high-voltage operation of nickel-rich oxide/graphite cells. *J. Phys. Chem. Lett.*, **12**, 4327-4338 (2021).
8. Gilbert, J. A., Shkrob, I. A., & Abraham, D. P. Transition metal dissolution, ion migration, electrocatalytic reduction and capacity loss in lithium-ion full cells. *J. Electrochem. Soc.*, **164**, A389 (2017).
9. Klein, S. et al. Exploiting the Degradation Mechanism of NCM523 Graphite lithium‐ion full cells operated at high voltage. *ChemSusChem*, **14**, 595-613 (2021).
10. Harlow, J. E. et al. A wide range of testing results on an excellent lithium-ion cell chemistry to be used as benchmarks for new battery technologies. *J. Electrochem. Soc.*, **166**, A3031 (2019).
11. Gilbert, J. A. et al. Cycling behavior of NCM523/graphite lithium-ion cells in the 3–4.4 V range: diagnostic studies of full cells and harvested electrodes. *J. Electrochem. Soc.*, **164**, A6054 (2016).
12. Zang, X. F., Sun, S., Yu, H., Yang, S., & Xia, H. L. The performances and degradation mechanisms of a commercial artificial graphite/$LiNi_{0.5}Co_{0.2}Mn_{0.3}O_2$ pouch cell at different cutoff voltages and temperatures. *J. Alloys Compd.*, **872**, 159678 (2021).
13. Lei, Q. et al. Lithium difluorophosphate as a multi-functional electrolyte additive for 4.4 V $LiNi_{0.5}Co_{0.2}Mn_{0.3}O_2$/graphite lithium ion batteries. *J. Electroanal. Chem.*, **846**, 113141 (2019).
14. Yang, T. et al. Sulfur-containing $C_2H_2O_8S_2$ molecules as an overall-functional electrolyte additive for high-voltage $LiNi_{0.5}Co_{0.2}Mn_{0.3}O_2$/graphite batteries with enhanced performance. *J. Power Sources*, **470**, 228462 (2020).
15. Jung, R., Metzger, M., Maglia, F., Stinner, C., & Gasteiger, H. A.. Oxygen release and its effect on the cycling stability of $LiNi_xMn_yCo_zO_2$ (NMC) cathode materials for Li-ion batteries. *J. Electrochem. Soc.*, **164**, A1361 (2017).
16. Zhao, W. et al. Assessing long□term cycling stability of single□crystal versus polycrystalline nickel□rich NCM in pouch cells with 6 mAh cm^{-2} electrodes. *Small*, **18**, 2107357 (2022).
17. Jung, R., Strobl, P., Maglia, F., Stinner, C., & Gasteiger, H. A. Temperature dependence of oxygen release from $LiNi_{0.6}Mn_{0.2}Co_{0.2}O_2$ (NMC622) cathode materials for Li-ion batteries. *J. Electrochem. Soc.*, **165**, A2869 (2018).
18. Li, W. et al. Long-term cyclability of NCM-811 at high voltages in lithium-ion batteries: An in-depth diagnostic study. *Chem. Mater.*, **32**, 7796-7804 (2020).
19. Park, C. et al. Malonic-acid-functionalized fullerene enables the interfacial stabilization of Ni-rich cathodes in lithium-ion batteries. *J. Power Sources*, **521**, 230923 (2022).
20. Dai, P. et al. Synergistic effect of dual-anion additives promotes the fast dynamics and high-voltage performance of Ni-rich lithium-ion batteries by regulating the electrode/electrolyte interface. *ACS Appl. Mater. Interfaces*, **14**, 39927-39938 (2022).